

Mechanical and fracture behavior of insulating refractory bricks

A. Mocciano^{1*}, J. M. Martínez^{1,2}, P. V. López^{1,2}, M. S. Conconi^{1,2}, N. M. Rendtorff^{1,2}

¹Centro de Tecnología de Recursos Minerales y Cerámica (CIC-CONICET La Plata),

Cno. Centenario y 506, 1897, M.B. Gonnet, Argentina

²Departamento de Química, Facultad de Ciencias Exactas,

Universidad Nacional de La Plata, La Plata, Argentina

Abstract

Microstructure, texture, and mechanical and fracture characterization of three insulating commercial refractories were carried out in order to establish a correlation between these properties. The materials were characterized using X-ray powder diffraction (XRD) with Rietveld and Le Bail approximation to perform phase quantification, mercury intrusion porosimetry, and scanning electron microscopy. The mechanical behavior of insulating commercial refractories was studied with a multi-technique approach that involved a three-point bending test, uniaxial compression test, and single-edge notched beam (SENB) test. Stable fracture tests were successfully performed. The obtained results showed that the main differences between the materials studied were pore size distribution and mineralogical composition. Materials with the major amount of mullite had the highest values of the mechanical parameters in the different performed tests.

Keywords: mechanical properties, fracture toughness, microstructure, refractories.

INTRODUCTION

Refractory materials are expected to withstand different degrees of thermal and mechanical stress during service. Several applications of refractory materials can be achieved according to the raw materials and the processing used. The performance of refractories during service is related to chemical composition, microstructure, and texture [1]. Industries involving processes at high temperatures (≥ 1000 °C) require insulating refractories to reduce energy consumption and make efficient use of energy [2]. This type of refractory usually has high porosity coupled with low thermal conductivity values ($< 1 \text{ W}\cdot\text{m}^{-1}\cdot\text{K}^{-1}$) [3, 4]. Depending on the process conditions, insulating materials can be directly in contact with the heat source or in a secondary layer beside dense refractories, ordinarily with a metal backup (steel or stainless steel). During service, this type of refractory is submitted to thermal and mechanical loads, the latter usually of the compressive type. Additionally, during storage, transport, and installation, refractories could be subjected to more complex types of mechanical loads. Although their mechanical properties are not critical properties, they must be adequate for their industrial application.

In general, the studies found in the literature analyze the mechanical behavior of these refractory materials under compressive stress [5, 6]. To the best of the authors' knowledge, there are no deep studies correlating the mechanical and fracture behavior of insulating refractory

materials with their micro and macro-characteristics. In particular, high porosity values result in better overall thermal properties while usually deriving in less dense and less mechanically resistant materials [7, 8]. A compromise between these two properties is generated that must be tailored or selected to produce a suitable refractory material or lining. Porous ceramics are used in a large number of applications and they are manufactured by different strategies from a wide variety of raw materials [9, 10]. The relationship between the microstructure and the properties of porous ceramics has been studied in different works [11-14]. However, there is still a need to predict the properties of ceramic materials with complex systems that present a variety of shapes, distribution, and amount of pores as well as a variety of distribution and amount of crystalline or non-crystalline phases.

The aim of this work is to analyze and correlate the mechanical and fracture properties with the microstructure of three insulating commercial refractories. A good understanding of the material's mechanical properties and the relation with their micro and macrostructure can be used for the future design and development of refractories with technological applications.

MATERIALS AND METHODS

Materials: three insulating commercial refractory bricks were studied. The selection of commercial materials has the advantage to avoid issues related to the manufacturing process and the reproducibility of materials, while also ensuring their appropriate thermal properties for their use as insulating refractories. The materials used in this study

*anamocciano@cetmic.unlp.edu.ar

 <https://orcid.org/0000-0001-7764-067X>

were JM23, JM26, and JM28 (Morgan Adv. Mater.). The maximum temperature to use these insulating refractories are 1260, 1430, and 1540 °C, respectively. The chemical composition of the three materials taken from the technical datasheet is shown in Table I. Material JM28 presented the highest amount of alumina meanwhile material JM23 had the highest amount of silica. Calcium oxide was only present in a considerable percentage in the material JM23. Density values informed in the datasheet were 480, 800, and 890 kg/m³ for JM23, JM26, and JM28, respectively.

Table I - Chemical composition (wt%) of the insulating refractories.

Oxide	JM23	JM26	JM28
Al ₂ O ₃	37.0	58.0	67.1
SiO ₂	44.4	38.8	30.0
Fe ₂ O ₃	0.8	0.8	0.6
TiO ₂	1.2	0.3	0.5
CaO	15.2	0.1	0.1
MgO	0.3	0.2	0.1
Na ₂ O+K ₂ O	1.1	1.7	0.9

Materials characterization: crystalline phases were analyzed by X-ray diffraction (XRD, D2 Phaser, Bruker) with CuK α radiation and Ni filter, at 30 kV-10 mA. XRD patterns were analyzed with the software FullProf (v.6.0), which is a multipurpose profile-fitting program, including the Rietveld method to perform phase quantification. The amorphous phase was quantified by the Le Bail approach, in which this phase is introduced in the refinement as crystalline silica with extremely low crystallite size [15, 16]. Open pore size distribution was evaluated by mercury intrusion porosimetry (Pascal 440, Thermo Scient.). Microstructure was analyzed by scanning electron microscopy (SEM, JCM 6000, Jeol).

Mechanical and fracture characterization: prismatic bars of 30x30x115 mm and cubes of 50x50x50 mm were diamond machined from the received bricks for the evaluation of their mechanical properties at room temperature using different methods. At least eight samples for each material were tested for each test and an average value was informed. The stress-strain and load-displacement curves obtained in each test were also analyzed. The flexural strength of the prismatic bars was measured by the three-point bending test in a universal testing machine (mod. 598, Instron) at a displacement rate of 0.5 mm.min⁻¹. In addition, the compressive strength of the cubes was determined with the same universal testing machine with steel plates, at a constant rate of 0.5 mm.min⁻¹. For each test, the following mechanical parameters were determined from the stress-strain curves: apparent Young's modulus (E) as the slope of the first linear part of the stress-strain curve ($\epsilon < 0.003$) and fracture (or mechanical) strength considering the maximum stress as the failure criterion. Depending on the test, this parameter (strength) is the modulus of rupture (MOR)

or the cold crushing strength (CCS). The dynamic elastic modulus (E_{dyn}) was also determined at room temperature by the impulse excitation technique (MK5 Industrial, GrindoSonic). Measurements were made on prismatic bars (30x30x115 mm). Single-edge notched beam (SENB) test was used to evaluate the fracture toughness (K_{IC}) of the three materials. Prismatic bars (30x30x115 mm) with notches 0.4 mm wide and 12 mm depth were used for this test; the samples were center notched with a diamond hacksaw. K_{IC} values were calculated by:

$$K_{IC} = \frac{3Q.L.C^{1/2}}{2W.D^2} \left[A_0 + A_1 \left(\frac{C}{D} \right) + A_2 \left(\frac{C}{D} \right)^2 + A_3 \left(\frac{C}{D} \right)^3 + A_4 \left(\frac{C}{D} \right)^4 \right] \quad (A)$$

where Q is the load applied to the notched bar, L is the span, C is the depth of the notch, D is the thickness of the specimen, W is the width of the specimen, and $A_0, A_1, A_2, A_3,$ and A_4 are functions of the ratio (L/D) [17]. Work of fracture (γ_{WOF}) was determined considering the area (energy) under load (Q)-displacement (e) curve, obtained in the SENB test, divided by twice the fracture surface area (A) [18]:

$$\gamma_{WOF} = \frac{\int Qde}{2A} \quad (B)$$

RESULTS AND DISCUSSION

Crystallographic characterization: diffraction patterns of the materials are shown in Fig. 1. JM23's main crystalline phase was plagioclase, with some peaks associated with mullite. Meanwhile, for JM26 and JM28 mullite was their main crystalline phase, presenting both also alumina (α -Al₂O₃) as a secondary phase. Fig. 2 shows the phase composition evaluated by the Rietveld method and Le Bail approximation. As was observed by XRD, JM28 presented the highest amount of mullite and this was related to the amount of alumina and silica shown in the chemical composition.

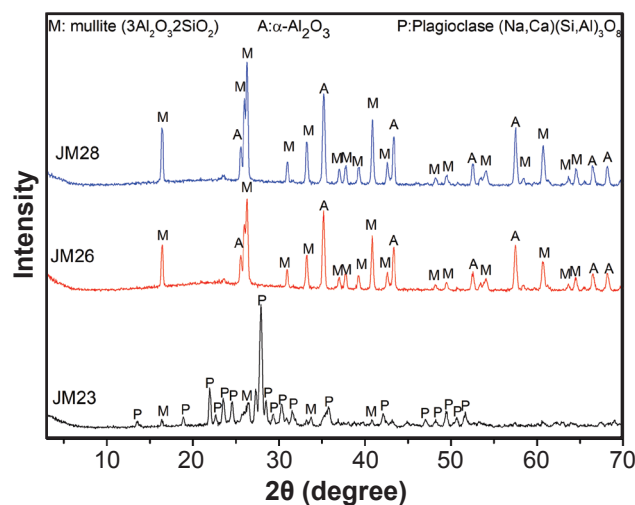


Figure 1: XRD patterns of the insulating commercial refractories. Peaks were identified using reference data: mullite (M) PDF 01-079-1454; α -Al₂O₃ (A) PDF 01-083-2080; and plagioclase (P) PDF 00-041-1486.

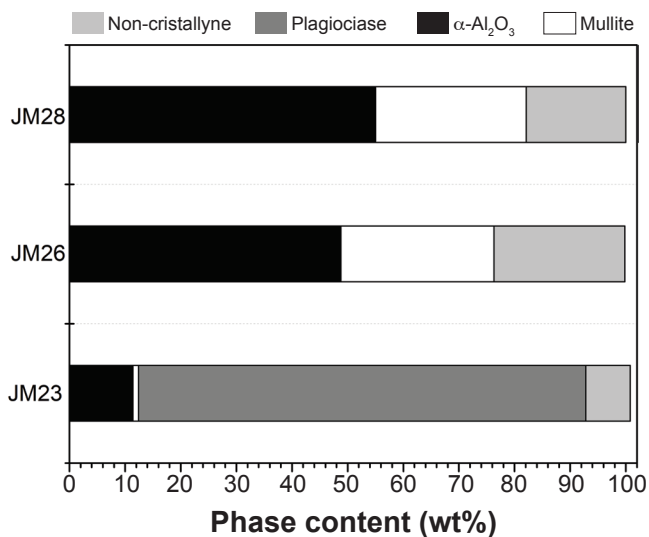


Figure 2: Results of Rietveld’s phase quantification of JM23, JM26, and JM28 materials.

For the non-crystalline phase in JM23, an attempt to use the Le bail approximation was done but ultimately discarded, as the overlapping of the plagioclase peaks interfered with the modeling of the amorphous band. However, the amount of non-crystalline phase could be approximated using the percentage of calcium reported in the technical datasheet as an upper limit of the amount of plagioclase in the material. Based on this, the percentages of all crystalline and non-crystalline phases of JM23 were recalculated as 80.4 wt% of plagioclase, 11.4 wt% of mullite, and 8 wt% of non-crystalline phases. No significant differences were found between the refined cell parameters of the crystalline phases obtained by the Rietveld method and those published in the literature [19-21].

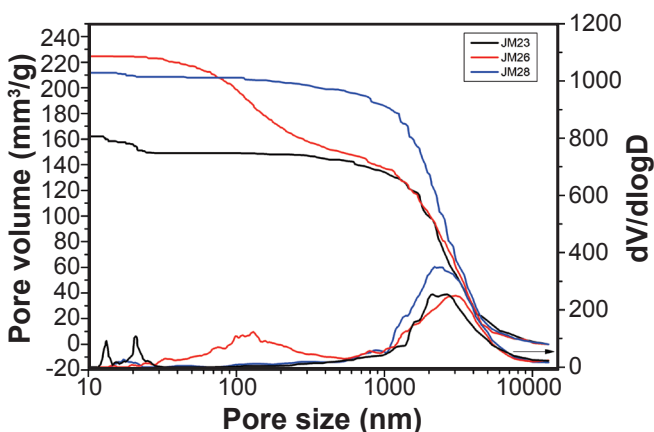


Figure 3: Pore size distribution curves of the insulating commercial refractories.

Table II - Pore sizes (diameters) of the materials.

Pore size	JM23	JM26	JM28
d_{10} (nm)	5360	4150	4550
d_{50} (nm)	2320	1720	2360
d_{90} (nm)	340	90	800

Microstructural analysis: pore size distribution curves of the insulating commercial refractories are shown in Fig. 3 and the pore size percentiles are presented in Table II. JM26 presented a bimodal pore size distribution while JM23 and JM28 exhibited monomodal distributions. JM28 presented pores in the range of 1000-10000 nm and JM23 presented pores in the range of 700-3200 nm. On the other hand, JM26 presented pores in two ranges one between 30-300 nm and the other between 700-3200 nm. The signals below 20 nm were considered spurious peaks related to the detection limit zone of the equipment. The mean pore size (d_{50}) did not vary considerably within the studied materials and corresponded to ~2000 nm (Table II). It is also worth pointing out that the three materials presented an almost equivalent upper limit of the pore distribution, below 5 μ m.

Digital and SEM images for the three materials are shown in Fig. 4. Different pore sizes are observed in SEM images. As was observed in Fig. 3, JM26 showed a greater proportion of pores than the other materials. Digital images revealed a rough, highly porous surface for JM26 and JM28, with pore sizes up to 1.0 mm. Meanwhile, JM23 had a somehow smoother surface and, albeit having a high surface porosity, pore size was shown to be at 0.5 mm at most. Rounded pores were observed in JM23 and pores without defined shapes in JM26 and JM28. Fig. 5 presents a high-magnification image of the JM28 sample. According to these micrographs, the samples presented a glassy continuous phase with some grains embedded into it. Particularly, several mullite needles were identified inside the matrix of JM28, as can be clearly

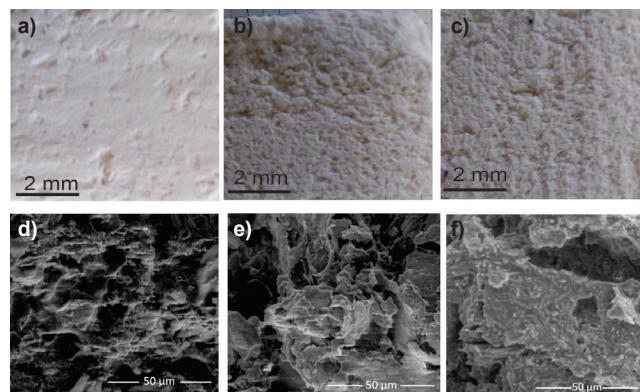


Figure 4: Digital images of the sample surface (a,b,c) and SEM images of fracture surface (d,e,f) of JM23 (a,d), JM26 (b,e), and JM28 (c,f).

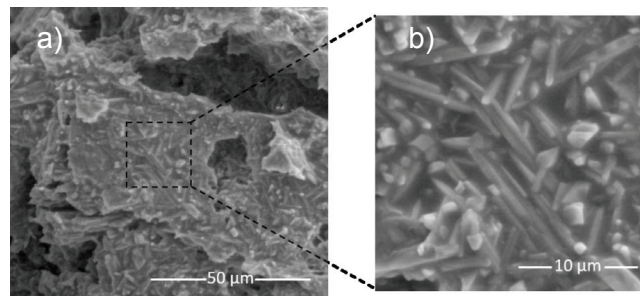


Figure 5: SEM images of JM28 with different magnifications.

observed in the zoomed image of Fig. 5b. No preferential orientation of the mullite needles was observed.

The volume fraction composition of microconstituents for each material is shown in Fig. 6. These values were estimated considering Rietveld phase quantification, theoretical densities reported in the literature, and materials density [17] informed in the datasheet. The JM26 and JM28 presented almost 70% of pore volume while JM23 showed 64% of pore volume. The solid phase volume of the JM28 and JM26 was 15% and 17% of mullite in each case and a fraction <15% of non-crystalline and alumina phases, the non-crystalline phase being slightly higher for the JM26. These percentages of porosity were consistent with the thermal conductivity values ($0.12\text{--}0.4\text{ W}\cdot\text{m}^{-1}\cdot\text{K}^{-1}$) reported in the datasheet and with similar insulating ceramics [22, 23]. On the other hand, the solid phase volume of the JM23 was 30% of plagioclase, and less than 6% of mullite and non-crystalline phase. The amount of porosity was more than 60% for all studied materials, thus implying that the main difference between the three materials was their mineralogical composition and the pore size and shape distributions. In this type of silico-aluminate materials, the mullite hypothesis for strength can be considered. In general, it is expected that material with more amount of mullite crystals improve their mechanical properties [19, 24].

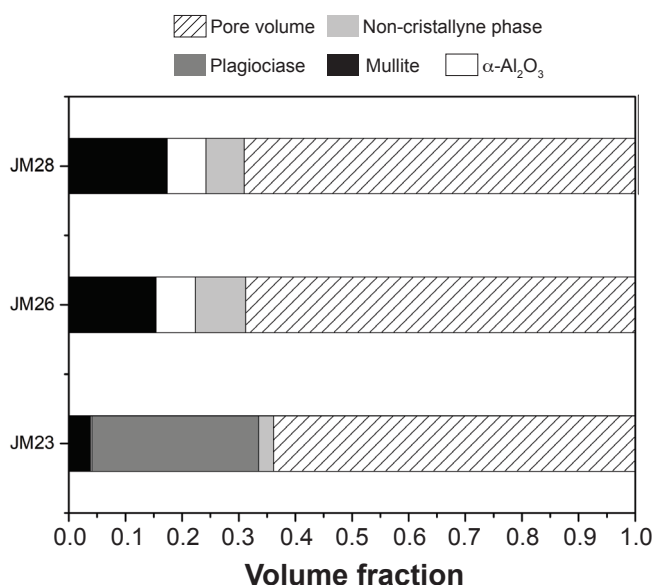


Figure 6: Volume fraction composition of microconstituents for the JM23, JM26, and JM28 materials.

Mechanical and fracture properties: typical stress-strain curves for flexural and compressive tests are shown in Figs. 7a and 8a, respectively. In these figures, a model curve for porous ceramics is shown [25]. In the case of the flexural test, there is first a linear zone, then the fracture zone, and finally, a zone related to semi-stable fracture at the tail of the curve (Fig. 7b). Flexural behavior of JM26 and JM28 showed first a linear zone until the sudden fall of the load followed by a semi-stable fracture [18]. The end of the curve of the JM23 was different from the other materials

and corresponded to fragile fracture typically for brittle materials [26]. In addition, the linear zone was different for the materials studied. JM23 presented a clearly linear relation between strain and stress. On the other hand, JM26 and JM28 showed a first linear stress-strain relationship until strain (ϵ) values less than 0.003, then a transitional deviation from linearity, and finally a linear behavior was recovered prior to the fracture point. It can be concluded that the three materials presented a reversible behavior for values of strain less than 0.003 corresponding to a linear elastic zone. The compressive stress model curve (Fig. 8b) first has a linear zone and after fracture, a slight drop in load, followed by an extended region where strain increases continuously and stress remains almost constant [27]. Amplification of the rupture zone is present as an inset in Fig. 8a where differences among materials are observed. JM28 curve showed a more abrupt drop in load after fracture than the other materials. From these tests, several mechanical and fracture parameters were calculated; modulus of rupture (MOR), cold crushing strength (CCS), and apparent Young's modulus of each test are summarized in Table III. Controlled stable fracture testing on brittle materials is difficult to perform [28]. The relative standard deviation of the parameters was between

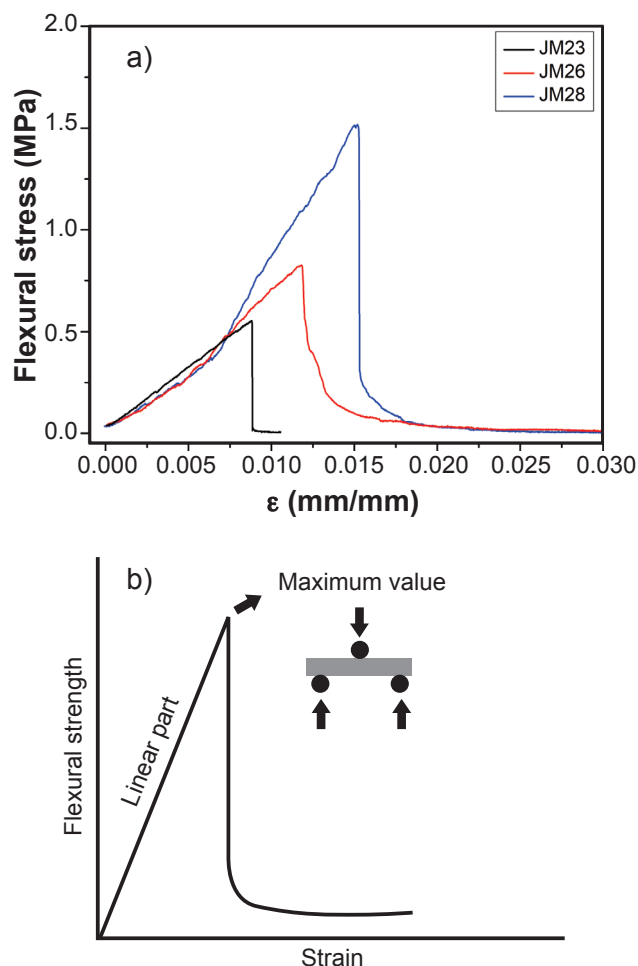


Figure 7: Flexural stress-strain curves of materials JM23, JM26, and JM28 (a) and a model curve (b).

8% and 26%; these values are in agreement with those reported in the literature on mechanical parameters [7]. Particularly, JM26 presented higher deviations.

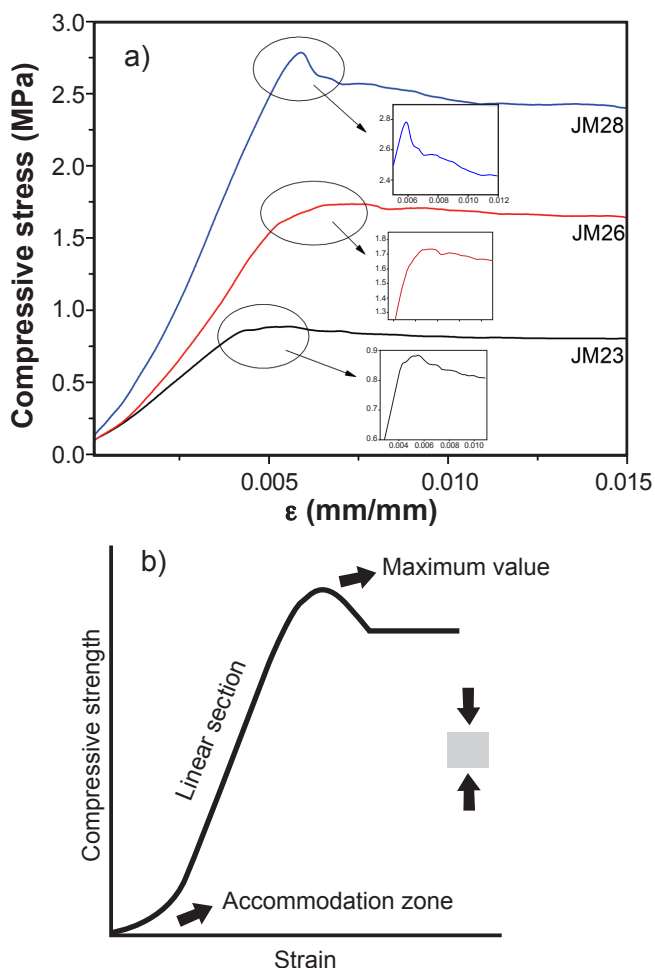


Figure 8: Compressive stress-strain curves of materials JM23, JM26, and JM28 (a) and a model curve (b).

The same trend was observed for the modulus of rupture and cold crushing strength of the materials. The material with less porosity (JM23) had the lowest mechanical parameters and the largest values for such parameters were found for JM28. In the literature, it is frequent to relate strength and porosity by an exponential equation, as proposed by Rice [29], which presents a gradual decrease of the mechanical property as a function of the porosity. This decrease is attenuated in high values of porosity approaching asymptotically zero. Particularly, the samples studied in this work present similar porosities (64-70%, Fig. 6) leading to the same region in mechanical resistance vs. porosity plot [30, 31], where mechanical properties do not change significantly by porosity, in agreement with Rice's model. The JM28 case, where the mechanical performance is quite different (slightly larger strength values compared to the other samples), is also the sample with the highest mullite amount. So, its mechanical behavior differences may be attributed to the crystalline composition. In this respect, mullite materials are widely studied and used due to their favorable thermal and mechanical properties [20, 24, 32-35].

Fig. 9 correlates the different mechanical parameters obtained in flexural and compressive tests. It can be observed that all the evaluated parameters had a direct relationship with each other. In general, a monotonic increasing relationship was found between the quantities in all the plots. In order to show this, straight dash lines are included in the figures for visual guidance. The value of the compressive strength was three times greater for JM28 than JM23 and in the case of the flexural strength, this ratio was 2.6. Otherwise, apparent Young's modulus values were 2.6 and 3 times greater for JM28 than JM23 for the compressive and flexural tests, respectively.

In order to estimate the stability and durability of refractories, a key factor is fracture mechanical characterization. In this aspect, the fracture test can

Table III - Type of fracture, apparent Young's modulus (E), modulus of rupture (MOR), and cold crushing strength (CCS) of the studied materials.

Parameter		JM23	JM26	JM28
Type of fracture	Flexural strength	Fragile	Semi-stable	Semi-stable
	SENB	Stable	Semi-stable	Semi-stable
Compressive test	CSS (MPa)	0.83	1.4	2.3
	Coefficient of variation (%)	11	15	12
	E_c (GPa)	0.14	0.22	0.37
	Coefficient of variation (%)	23	16	5
Flexural test	MOR (MPa)	0.54	0.80	1.4
	Coefficient of variation (%)	15	18	8
	E_f (GPa)	0.03	0.08	0.10
	Coefficient of variation (%)	23	26	13
Dynamic elastic modulus test	E_{Dyn} (GPa)	2.3	2.2	2.3
	Coefficient of variation (%)	13	26	13

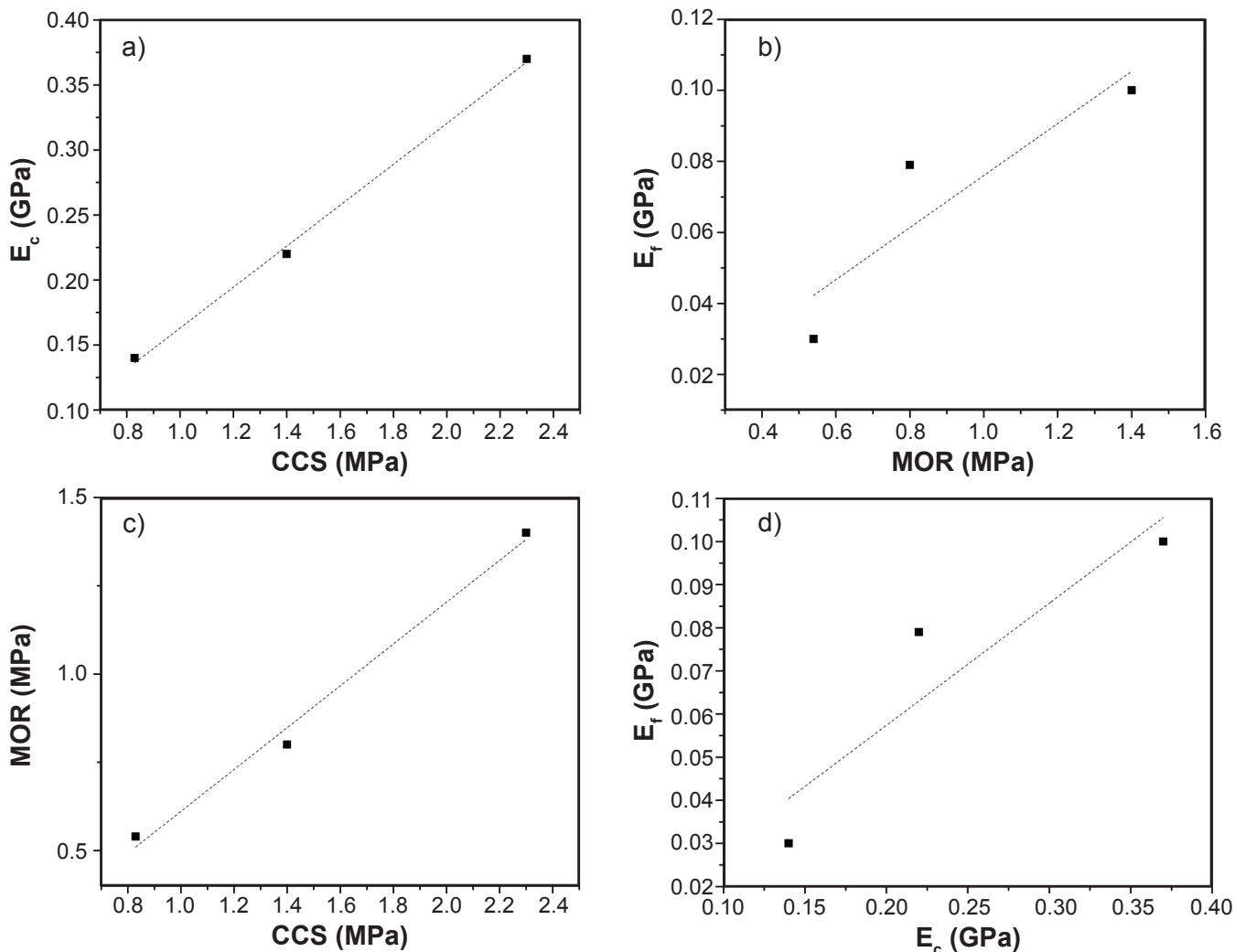


Figure 9: Apparent Young's modulus in compression (E_c) as a function of CCS (a), apparent Young's modulus in flexure (E_f) as a function of MOR (b), MOR as a function of CCS (c), and E_f as a function of E_c (d).

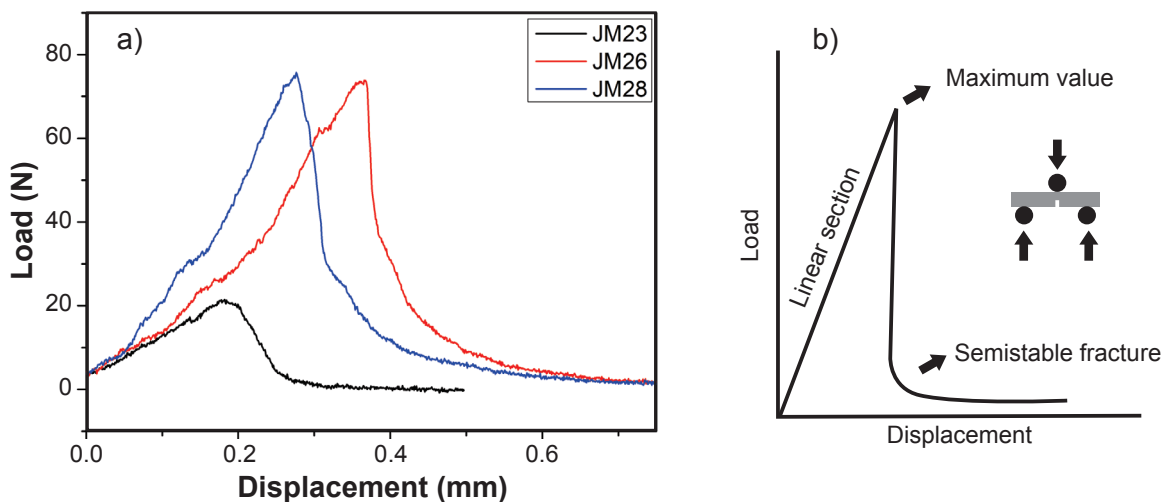


Figure 10: Characteristic load versus displacement curve in the SENB test of materials JM23, JM26, and JM28 (a) and a model curve (b).

provide additional phenomenological insights into ceramic mechanical behavior. Determination of fracture toughness and work of fracture parameters by the single-edge notched

beam test is one of the friendliest methods used in the literature [36-39]. However, this type of test is difficult to carry out on refractories because it is necessary to achieve

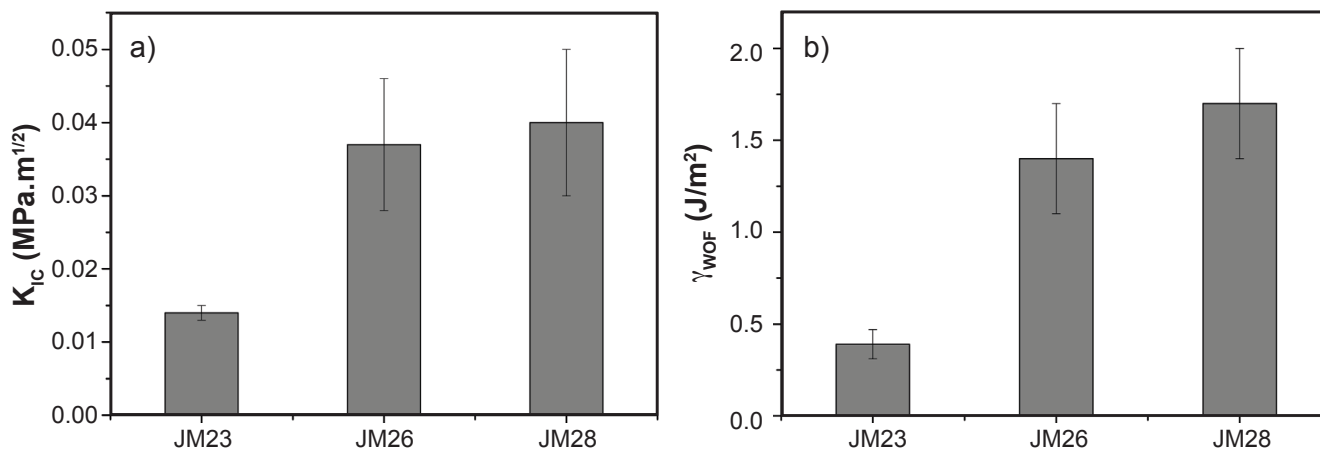


Figure 11: Average toughness parameters for the studied materials: a) critical stress intensity factor in mode I, K_{IC} ; and b) work of fracture, γ_{WOF} .

stable crack propagation and to monitor energy demands during propagation [25]. Fig. 10a shows characteristic load-displacement curves in the SENB test for each of the studied materials and Fig. 11 shows the average values of toughness parameters. The model of the load-displacement curve (Fig. 10b) first has a linear elastic region, then the fracture zone, and finally a long tail in the region of decreasing load related to the semi-stable fracture [40]. The three materials' load-displacement characteristic curves showed irregularities in the linear zone related to irreversible mechanical failures in the microstructure; this behavior was observed for highly porous ceramic foams and has already been reported [41]. As a result, the curve can be described as the envelope of many micro-cracks and the parameters determined in this test are globally representative of all these processes. The characteristic curves of the SENB test of JM28 and JM26 were similar, with similar maximum load values; both materials had a semi-stable fracture. On the other hand, the SENB test characteristic curve of JM23 showed a stable fracture.

The largest values of K_{IC} corresponded to JM28 and JM26, and the lowest value was for JM23; the same trend was observed for the work of fracture (Fig. 11). For JM26 and JM28, K_{IC} values were more than 2.5 times greater than for JM23 (Fig. 11a). This contrast between samples was also observed in γ_{WOF} values (Fig. 11b). The relative standard deviation of K_{IC} and γ_{WOF} values were around 25% and 20%, respectively. As in the compressive and three-point bending tests, the materials with high mullite content (JM26 and JM28) presented the highest values of mechanical parameters. Also, it showed that porosity was not the main factor affecting mechanical properties and fracture mechanisms within these high-porosity materials.

CONCLUSIONS

The mechanical and fracture behavior of insulating commercial refractories was studied with a multi-technique approach. The studied materials are designed for different temperatures of service. However, the pore volume fraction for the studied materials was similar (60-70%) and the

main differences were the pore size distribution and the mineralogical composition. Stable fracture characterization was performed by a single-edge notched beam test. Fracture toughness and work of fracture were calculated from these evaluated stable curves. A well-defined semi-stable fracture mechanism was observed and described taking into account the mineralogical composition and the microstructure of the materials. A monotonic correlation was observed for all the calculated mechanical and fracture parameters within this family of materials: compressive and flexural strength, stiffness, and toughness and work of fracture. Materials with mullite (JM26 and JM28) as the main crystalline phase, which present higher refractoriness, presented the highest values of the mechanical and fracture parameters in the different tests.

ACKNOWLEDGMENTS

This work was partially supported by Facultad de Ciencias Exactas, Universidad Nacional de La Plata (UNLP, X-877, and X-904), and CETMIC. JMM and PVL thank CONICET for the fellowships; AM and NMR are members of CONICET. The authors also wish to thank Ricardo Anaya for helping us with the SEM images and Diego Richard for the final comments on the manuscript.

REFERENCES

- [1] C.B. Carter, M.G. Norton, *Ceramic materials: science and engineering*, Springer, New York (2013).
- [2] G. Deshmukh, P. Birwall, R. Datir, S. Patel, J. Food Process. Technol. **8**, 4 (2017) 670.
- [3] J. Ma, F. Ye, B. Zhang, Y. Jin, C. Yang, J. Ding, H. Zhang, Q. Liu, Ceram. Int. **44** (2018) 13320.
- [4] H. Liu, X. Xiong, M. Li, Z. Wang, X. Wang, Y. Ma, L. Yuan, Ceram. Int. **46** (2020) 14474.
- [5] M. Fukushima, Y. Yoshizawa, J. Eur. Ceram. Soc. **36** (2016) 2947.
- [6] B. Xia, Z. Wang, L. Gou, M. Zhang, M. Guo, Ceram. Int. **48** (2022) 10475.
- [7] S. Meille, M. Lomabardi, J. Chevalier, L. Montanaro, J.

- Eur. Ceram. Soc. **32** (2012) 359.
- [8] A.R. Studart, U.T. Gonzenbach, E. Tervoort, L.J. Gauckler, J. Am. Ceram. Soc. **89** (2006) 1771.
- [9] E.C. Hammel, O.L.R. Ighodaro, O.I. Okoli, Ceram. Int. **40** (2014) 15351.
- [10] Y. Chen, N. Wang, O. Ola, Y. Xia, Y. Zhu, Mater. Sci. Eng. R **143** (2021) 100589.
- [11] T. Shimizu, K. Matsuura, H. Furue, K. Matsuzak, J. Eur. Ceram. Soc. **33** (2013) 3429.
- [12] M.L. Sandoval, M.A. Camerucci, A.G. Tomba Martinez, J. Mater. Sci. **47** (2012) 8013.
- [13] V.R. Salvini, V.C. Pandolfelli, D. Spinelli, in "Recent advances in porous ceramics", U.M.B. Al-Naib (Ed.), InTech (2018) 171.
- [14] M.F. Hernández, G. Suárez, M. Cipollone, E.F. Aglietti, N.M. Rendtorff, Ceram. Int. **43** (2017) 11759.
- [15] M.S. Conconi, M.R. Gauna, M.F. Serra, G. Suárez, E.F. Aglietti, N.M. Rendtorff, Cerâmica **60**, 356 (2014) 524.
- [16] A. Le Bail, J. Non-Cryst. Solids **183** (1995) 39.
- [17] N.M. Rendtorff, E.F. Aglietti, Mater. Sci. Eng. A **527** (2010) 3840.
- [18] A. García-Prieto, C. Baudín, J. Eur. Ceram. Soc. **30** (2010) 3297.
- [19] M.F. Hernández, M.S. Conconi, M. Cipollone, M.S. Herrera, N.M. Rendtorff, Appl. Clay Sci. **146** (2017) 380.
- [20] H. Schneider, J. Schreuer, B. Hildmann, J. Eur. Ceram. Soc. **28** (2008) 329.
- [21] G. Fiquet, P. Richet, G. Montagnac, Phys. Chem. Miner. **27** (1999) 103.
- [22] F. Yang, C. Li, Y. Lin, C.A. Wang, Mater. Lett. **73** (2012) 36.
- [23] W. Zhou, Z. Zhang, N. Li, W. Yan, G. Ye, Ceram. Int. **48** (2022) 20721.
- [24] M. Romero, J.M. Pérez, Mater. Constr. **65**, 320 (2015) e065.
- [25] H. Harmuth, K. Rieder, M. Krobath, E. Tschegg, Mater. Sci. Eng. A **214** (1996) 53.
- [26] A. Wang, Y. Wang, C. Zhang, T. Zhang, H. Liao, Theor. Appl. Fract. Mech. **103** (2019) 102273.
- [27] W. Huo, X. Zhang, Y. Chen, Y. Lu, J. Liu, S. Yan, J.M. Wu, J. Yang, J. Eur. Ceram. Soc. **38** (2018) 2035.
- [28] J. Nakayama, H. Abe, R.C. Bradt, J. Am. Ceram. Soc. **64** (1981) 671.
- [29] R.W. Rice, Key Eng. Mater. **115** (1995) 1.
- [30] J. Sun, Z. Hu, J. Li, H. Zhang, C. Sun, Ceram. Int. **40** (2014) 11787.
- [31] K. Mohanta, A. Kumar, O. Parkash, D. Kumar, J. Eur. Ceram. Soc. **34** (2014) 2401.
- [32] M.F. Serra, M.S. Conconi, M.R. Gauna, G. Suárez, E.F. Aglietti, N.M. Rendtorff, J. Asian Ceram. Soc. **4** (216) 61.
- [33] M. Hamdouche, N. Bouaouadja, C. Olagnon, G. Fantozzi, Ceram. Int. **29** (2003) 599.
- [34] W. Zhou, W. Yan, N. Li, Y. Lin, Y. Dai, B. Han, Y. Wei, Ceram. Int. **44** (2018) 22950.
- [35] J. Martín-Márquez, J.M. Rincón, M. Romero, J. Eur. Ceram. Soc. **30** (2010) 1599.
- [36] R.C. Bradt, Key Eng. Mater. **88** (1993) 165.
- [37] N.M. Rendtorff, L.B. Garrido, E.F. Aglietti, Ceram. Int. **35** (2009) 2907.
- [38] V.R. Salvini, V.C. Pandolfelli, R.C. Bradt, Ceram. Int. **38** (2012) 5369.
- [39] S. Bueno, M.H. Berger, R. Moreno, C. Baudín, J. Eur. Ceram. Soc. **25** (2008) 1961.
- [40] A. García-Prieto, M.D. Ramos-Lotito, D. Gutiérrez-Campos, P. Pena, C. Baudín, J. Eur. Ceram. Soc. **35** (2015) 1955.
- [41] B.S.M. Seeber, U.T. Gonzenbach, L.J. Gauckler, J. Mater. Res. **28** (2013) 2281.
- (Rec. 11/10/2022, Rev. 27/12/2022, 22/02/2023, Ac. 28/02/2023)